Nano Research
2019, 12(12): 3109–3115

ISSN 1998-0124 CN 11-5974/O4
https://doi.org/10.1007/s12274-019-2562-x

Research Article

Bottom-up fabrication of graphitic carbon nitride nanosheets modified with porphyrin via covalent bonding for photocatalytic H_2 evolution

Shufang Tian, Sudi Chen, Xitong Ren, Ronghui Cao, Haiyan Hu, and Feng Bai (✉)

Key Laboratory for Special Functional Materials of Ministry of Education, National & Local Joint Engineering Research Center for High-efficiency Display and Lighting Technology, School of Materials Science and Engineering, and Collaborative Innovation Center of Nano Functional Materials and Applications, Henan University, Kaifeng 475004, China

Received: 25 September 2019 / **Revised:** 24 October 2019 / **Accepted:** 4 November 2019

ABSTRACT

In order to broaden the absorption range of graphitic carbon nitride, one of the common methods is to couple the well-known photosensitizer porphyrin with graphitic carbon nitride through van der Waals weak interactions. To date, to combine porphyrin with graphitic carbon nitride through covalent interactions has not been settled. In this work, through rational molecular design, we successfully incorporated porphyrin into the matrixes of graphitic carbon nitride by covalent bonding via one-pot thermal copolymerization. The resultant material not only can widen the absorption range but also possess the enlarged specific surface area and construction intramolecular heterojunctions which can contribute to improve electron-holes separation efficiency. The resultant photocatalyst exhibited enhanced H_2 production rate (7.6 mmol·g^{-1}·h^{-1}) and with the apparent quantum efficiency (AQE) of 13.3% at 450 nm. At the same time, this method opens a way to fabricate graphitic carbon nitride nanosheets via bottom-up strategy.

KEYWORDS

carbon nitride nanosheet, porphyrin, photocatalytic hydrogen evolution, covalent bonding

1 Introduction

Photocatalytic H_2 evolution is one of the promising ways to convert solar energy into clean and sustainable energy [1, 2]. Recent years, numerous semiconductor photocatalysts with enhanced activity have been developed [3–7]. Among which, the organic polymeric semiconductor graphitic carbon nitride (g-CN) has drawn broad attention owing to its suitable band gap for visible light response, its chemical and thermal stability, easy preparation and low-cost [8–13]. However, its limited visible light absorption ability, high recombination rates of photogenerated charge carriers and low specific surface area result in unsatisfactory photocatalytic capacity. Various modification methods have been developed to optimize its photocatalytic performance, including heteroatoms or organic molecular doping [14–17], nanostructure design [18–23], supramolecular assemble [24–26], exfoliation to nanosheets [27–29] and hybrid with other semiconductors or metal particles to form heterojunction structures [30–35].

Inspired by its intrinsic two-dimensional structure with repeating tri-s-triazine units bonded by amino group within in-plane direction and weak van der Waals forces between interlayers, many efforts have been made to fabricate two-dimensional graphitic carbon nitride nanosheets (CNNs). The unique merits of CNNs like larger specific surface area, enlarged bandgap and enhanced electron transport ability along in-plane direction [36, 37] make sure CNNs as excellent candidate for photocatalytic H_2 evolution. Two traditional strategies have been developed to fabricate CNNs, one is the top-down method which weakens the van der Waals forces between interlayers [38–40] and another is bottom-up approach that assembles the precursor molecules in two-dimensional patterns [41–44]. The former methods suffered from the time-consuming or low yield; the latter approaches were far from being fully studied. To develop new strategy to fabricate CNNs with broaden visible light response is meaningful and worthwhile.

Due to the excellent visible light absorption ability, porphyrins were widely used as photosensitizers or photocatalysts in photocatalytic reactions [45–49]. According to the former literatures, porphyrins always coupled with g-CN through weak interactions such as π–π stacking, hydrogen bonding and electrostatic interactions to form heterojunctions to improve photocatalytic properties [50–55]. As we known, the transfer of electrons will be greatly improved between g-CN and porphyrin through paths developed by the covalent bonds and the solar energy utilization efficiency would be improved [10, 51]. While it is still a great challenge to anchor porphyrin molecules on the g-CN framework through covalent bonding, because the limited absorption of porphyrin on the g-CN [10] and the quantity of amino group was too little to modify through conventional organic synthesis methods.

In this work, through rational molecular design, we choose 5,10,15,20-tetrakis (4-(2,4-diamino-1,3,5-triazinyl) phenyl)-porphyrin (TDPP) as the organic dopant to copolymerize with urea to fabricate the CNNs modified by TDPP through covalent bonding (Scheme 1). First, the supramolecular complexes can be easily formed via hydrogen bonding by mechanical mixing TDPP and urea before calcination (Fig. S1 in the Electronic Supplementary Material (ESM)). During the thermal polymerization process, the melted urea-TDPP solution could be formed at the temperature ranging from 150–300 °C [56], in which TDPP was uniformly dissolved in the solution in molecular state (Fig. S2 in the ESM). Based on Ref. [57], melamine was generated as reaction intermediate at temperatures of 234 °C,

Address correspondence to baifengsun@126.com

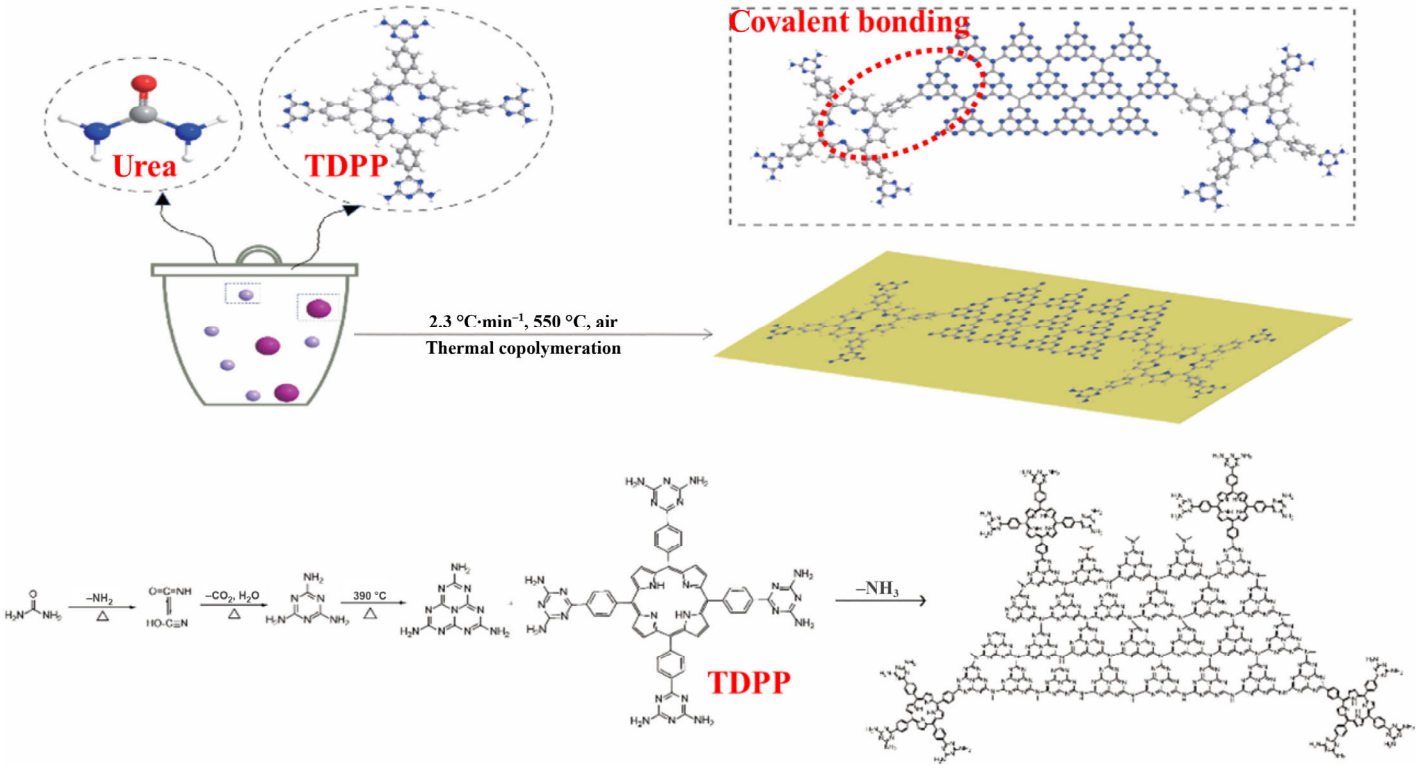

Scheme 1 Schematic illustration of the preparation process and the proposed copolymerization process of urea with TDPP.

which further copolymerized with 2,4-diamino-1,3,5-triazinyl group of TDPP at around 390 °C, accomplishing the fusion of TDPP into tri-*s*-triazine matrices via covalent bonding. The copolymerization process was similar to that reported before using other organic molecules bearing suitable groups as monomers [16, 17]. Meanwhile, the TGA test indicated there was no decomposition of TDPP at 390 °C (Fig. S3 in the ESM). When the temperature increased to 550 °C and kept for 2 h, the two-dimensional CNNs modified with TDPP were fabricated.

To our surprise, the resultant material can not only broaden the visible light absorption range but also can fabricate the CNNs with reduced thickness via the facile one-pot bottom-up method. At the same time, owing to the different electronic structure and chemical composition, the intramolecular heterostructures were constructed between TDPP with tri-s-triazines motifs, which were conductive to the charge separation and transportation. The photocatalytic H_2 production performance of the obtained material was 5 times as high as that of unmodified g-CNU which derived from pure urea thermal polymerization.

2 Experimental

2.1 The synthesis of TDPP

The porphyrin TDPP and its precursor 5,10,15,20-tetrakis(4-(4-cyano)phenyl)-porphyrin were synthesized according to the methods reported previously [58]. TDPP: ^{1}H NMR (DMSO-d_6, 400 MHz) 8.93 (s, 8H), 8.72–8.70 (d, J = 8 Hz, 8H), 8.35–8.33 (d, J = 8 Hz, 8H), 6.94 (s, 16H), −2.87 (s, 2H). Ultraviolet–visible (UV–Vis) absorption (dimethylformamided (DMF) solution): 421, 516, 552, 596, 649 nm.

2.2 The synthesis of g-CNU

The g-CNU nanosheets were synthesized according to the previously reported methods [57]. Briefly, 20 g urea was put into a crucible which half-covered with aluminum foil and heated to 550 °C for 2 h with a ramp rate of 2.3 °C·min^{-1} in air to fabricate the products, which was denoted as g-CNU.

2.3 The synthesis of g-CNU-TDPP

g-CNU-TDPP samples were synthesized by thoroughly mixing 20 g urea with different amounts (1, 3, 5, 10 or 20 mg) of TDPP under mechanical grinding by hand. The resultant supramolecular complexes were placed into a porcelain crucible which half-capped using aluminum foil as cover and calcined at 550 °C for 2 h with a heating rate of 2.3 °C·min^{-1} in a muffle furnace in air, the resultant nanosheets denoted as g-CNU-x mg TDPP (x = 1, 3, 5, 10, 20).

2.4 Material characterizations

The chemical structure of synthesized TDPP was confirmed by ^{1}H NMR using a Bruker AVANCE III HD 400M instrument. The crystalline phases of the as-obtained samples were characterized by X-ray powder diffraction (XRD), using Cu Kα radiation (λ = 0.154 nm) from a 40 kV X-ray source (Bruker D8 Advance) and the scanned 2θ ranged from 10° to 50°. Fourier transformed infrared (FT-IR) spectra were recorded using a VERTEX 70 FT-IR spectrometer and the wavenumber ranged from 500 to 4,000 cm^{-1}. X-ray photoelectron spectroscopy (XPS) measurements were performed on Thermo Scientific ESCALAB 250Xi system with a monochromatized Al Kα line source. The carbonaceous C 1s line at 284.6 eV was used as reference to calibrate the binding energies of other elements. Nitrogen adsorption–desorption isotherms were performed at 77 K using Quadrasorb SI-4 equipment. Before the measurements, the samples were degassed at 250 °C for 6 h to fully remove the absorbed compounds. Brunauer–Emmett–Teller (BET) method and Barrett–Joyner–Halenda (BJH) equation were applied to obtain the specific surface areas and pore size distributions of the as-prepared samples, respectively. The morphologies and microstructures of the samples were investigated by transmission electron microscopy (TEM) using a JEOL model JEM 2010 instrument. Atomic force microscopy (AFM) was recorded by a Bruker Dimension Icon system. The optical properties of the samples were measured by UV–Vis diffuse

reflectance spectroscopy (DRS) using a PerkinElmer Lambda 950 system. Steady and time-resolved fluorescence emission spectra of the samples were recorded at room temperature with a fluorescence spectrophotometer Edinburgh FLS980. The excitation wavelength was set to be 375 nm and it was probed at 460 nm.

2.5 Photoelectrochemical measurements

The photoelectrochemical measurements were conducted using a three-electrode cell (Autolab electrochemical workstation) with a Pt wire as counter electrode and a saturated Ag/AgCl as reference electrode. The working electrode was prepared by dip-coating method. The indium tin oxide (ITO) plate with the area of 2 cm^2 were cleaned by ultrasonication in deionized water and acetone for 30 min and then dried in air. About 1 mg of the photocatalyst was dispersed in 1 mL ethanol and 10 μL Nafion to form slurry and coated on the ITO plate with an exposure area of 1.5 cm^2 and dried in air. A 0.2 $mol·L^{-1}$ Na_2SO_4 aqueous solution (pH = 7.0) was chosen as the supporting electrolyte and was purged with N_2 to remove O_2 before any measurements. The electrochemical impedance spectroscopy (EIS) results were obtained at the open circuit potential using a frequency ranged from 10^5 Hz to 10^{-1} Hz. The Mott–Schottky plots were measured under different frequency (500, 1,000 and 1,500 Hz). The photocurrent density versus time was recorded under visible light switching on and off mode (λ > 400 nm, 300 W Xenon lamp).

2.6 Photocatalytic H_2 evolution evaluation

Photocatalytic H_2 production reactions were carried out in a 100 mL closed quartz flask reactor with top-irradiation model, which was sealed with seal rubber septa (Beijing China Education Au-Light Technology Co., Ltd,). Typically, 20 mg of the prepared photocatalyst powder were suspended in 50 mL aqueous solution containing of 10% triethanolamine (TEOA) as sacrificial agent with 2 wt.% Pt as cocatalyst which was *in situ* photo-deposited on the surface of the photocatalysts using K_2PtCl_6 as precursor. The system was vacuumed for 30 min, then the solution was irradiated by a 300 W Xenon lamp with UV-cutoff filter (λ > 400 nm) under continuous stirring and the reaction temperature was kept steadily at 6 °C by using a water-cooling filter. The hydrogen evolution was detected using an online gas chromatograph (GC-7920) equipped with a thermal conductivity detector (TCD), where nitrogen was used as the carrier gas. The long-time performance of the photocatalyst was tested as follows: The system was refreshed every 5 h and at last cycle 1 mL TEOA as sacrificial agent was added to check the reason for the declined photocatalytic ability. The wavelength dependent H_2 evolution rate was measured under 300 W Xenon lamp irradiation with different band-pass filters. The apparent quantum efficiency (AQE) was calculated according to the following equation

$$\mathrm{AQE}(\%) = \frac{\text{Number of reacted electrons}}{\text{Number of incident photons}} \times 100\%$$

$$= \frac{2 \times \text{number of evolved } H_2 \text{ molecues}}{\text{Number of incident photons}} \times 100\%$$

3 Results and discussion

3.1 Material characterization

First, the morphology and texture of g-CNU and g-CNU-TDPP were investigated by TEM images. As presented in Fig. 1, the dense and thick nanosheets with irregular holes of g-CNU (Fig. 1(a)) transformed into more thin, flat and transparent nanosheets with the size and thickness apparently reduced when modified by TDPP (Fig. 1(b)). The thickness of the nanosheets was further measured by AFM, comparing with the thickness of g-CNU nanosheets which was around 10 nm (Fig. 1(c)), the thickness of g-CNU-TDPP

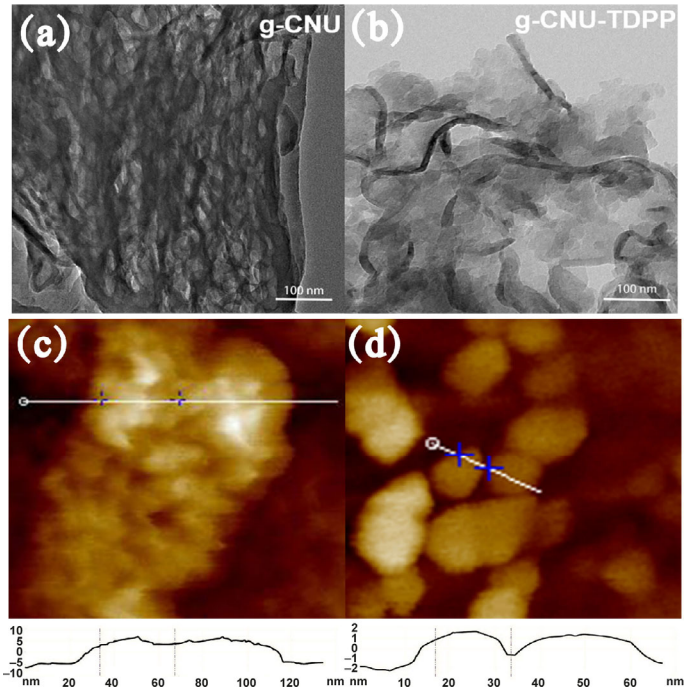

Figure 1 TEM images of (a) g-CNU and (b) g-CNU-TDPP and AFM image of (c) g-CNU and (d) g-CNU-TDPP.

nanosheets was reduced to 3 nm (Fig. 1(d)), which was in accordance with the observation from TEM images.

From the appearance, g-CNU-TDPP exhibited as loose and fluffy gray-white powders, contrasting to the yellow powder of g-CNU and the volume of g-CNU-TDPP with the same weight (300 mg) was much larger than that of g-CNU (Fig. 2(a), inset). The color change of g-CNU-TDPP showed a certain degree of blue-shift of absorption edge [38, 39] and fully indicated that TDPP altered the original polymerization way of urea. Nitrogen adsorption–desorption isotherms and corresponding pore size distribution curves were further carried out to examine the effect of TDPP on the specific surface area and mesopores distribution. The isotherms for g-CNU-TDPP and g-CNU both exhibited type IV behavior with an H1 type hysteresis loop (Fig. 2(a)). An obviously enhanced adsorption capacity at relative pressure P/P_0 > 0.8 was observed from the BET isotherm of g-CNU-TDPP, indicating the production of abundant mesopores. The BET surface area of g-CNU-TDPP was 165 $m^2·g^{-1}$, which was nearly 3-times that of g-CNU (58 $m^2·g^{-1}$). It can infer that the introduction of TDPP as co-monomer indeed promoted the generation of mesopores and lead to the increased specific surface area. Besides, the pore size distribution of g-CNU-TDPP mainly concentrated at 2 nm and the intensity of the peak greatly increased (Fig. 2(b)) comparing with g-CNU, the pore size of which distributed at 2 nm and 10–50 nm. The change may originate from the steric configuration of TDPP, which prevented further accumulation of the interlayer and altered the in-plane connectivity mode, leading to the enlarged specific surface area.

The crystal structure of the g-CNU-TDPP samples were analyzed by XRD pattern (Fig. S4(a) in the ESM). Two characteristic peaks of g-CNU located at about 13.5° and 27.8° were observed, corresponding to the (100) and (002) crystal planes, respectively [17]. As for g-CNU-TDPP samples, the intensity of (002) peaks were weakened and the peaks were slightly broadened when doping with TDPP, demonstrating the layered structure of g-CNU have been exfoliated to more thinner nanosheets [38], which was consistent the AFM analysis.

The chemical structure of the resultant samples was confirmed by FT-IR spectra. The spectra of g-CNU-TDPP samples were similar to that of g-CNU (Fig. S4(b) in the ESM). The sharp peak

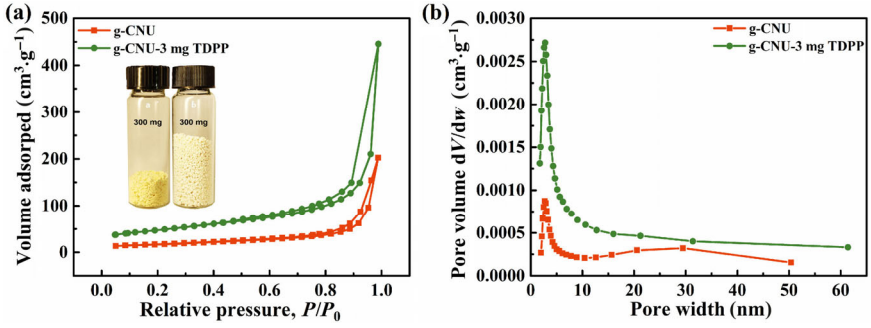

Figure 2 (a) N_2 adsorption–desorption isotherms and (b) corresponding BJH pore-size distribution of g-CNU and g-CNU-TDPP. Inset: optical photograph of the same weight of 300 mg g-CNU and g-CNU-TDPP.

at 807 cm^{-1} is ascribed to the breathing vibration of the heptazine units, the stretching vibration signals of aromatic CN heterocycles are presented in the range of 1,200–1,600 cm^{-1}, and the broad peaks between 3,000 and 3,500 cm^{-1} are contributed by the N–H stretching [17]. The peaks of TDPP not observed may be attributed to the majority peaks of TDPP located in the range of 1,000–1,600 cm^{-1}, which are overlapped with the strong peaks of g-CNU and the doping amount of TDPP (the maximum was 5%) was too low to be detected.

The chemical states of the g-CNU-TDPP were also investigated. High-resolution of carbon and nitrogen XPS analyses (Fig. S5 in the ESM) revealed that there was no pronounced distinction between g-CNU-TDPP and g-CNU, indicating the chemical states of g-CNU-TDPP were the same as g-CNU. The binding energy of C 1s located at 284.6 and 287.9 eV, which are attributed to the sp^2 C=C bonds and sp^2 hybridized carbon bonded to N (N–C=N) in the triazine rings. The peak located at 398.3 eV in the N1s spectra can be deconvoluted into two peaks. The dominant at 398.4 eV corresponds to the sp^2-bonded N (C–N=C) in the triazine rings, while the peak at 399.9 eV is ascribed to the bridging N atoms in $N–(C)_3$. The peaks at 400.7 and 404.2 eV are attributed to the amino groups and the charging effects [38].

The UV–Vis spectra showed that the optical edges of the modified g-CNU-TDPP samples were all obviously blue shift from 425 nm of pristine g-CNU to shorter wavelength (410–420 nm) with the incorporation of different amount of TDPP into the framework of g-CNU (Fig. 3(a)). This blue-shift tendency may be ascribed to the quantum confinement effect due to the reduced particle size and the thickness of g-CNU-TDPP nanosheets [38]. Simultaneously, the absorption tails extending to 700 nm gradually became stronger with the increasing content of TDPP, caused by the excellent optical absorption capacity of TDPP anchoring into the matrices of nanosheets. The optical bandgaps of the samples were estimated from plots of $(\alpha h\nu)^2$ versus photon energy (Fig. 3(a), inset). The interesting feature was that the energy bandgaps (E_g) were shifted from 2.99 to 3.03–3.04 eV when fusion of TDPP into the nanosheets matrices, but *E*g had little relationship with the doping amount.

The band structure of the g-CNU-TDPP was measured by a combined analysis of XPS valence band spectra and Mott-Schottky plots to determination the location of the valence bands (VB) and conduction bands (CB). The valence bands of g-CNU-TDPP and g-CNU located at 1.43 and 1.79 eV, respectively, according to the XPS valence band measurements (Fig. 3(b)). The Mott-Schottky plots under different frequencies revealed the n-type characteristic of g-CNU-TDPP based on the positive slope of the plots (Figs. 3(c) and 3(d)) [38]. The derived flat-band potential was about −1.81 V versus Ag/AgCl. It was negative shift of 0.41 V than that of g-CNU which located at −1.40 V versus Ag/AgCl. The negative movement of CB is conductive to the photocatalytic H_2 evolution because of the higher reduction ability of the photogenerated electrons. The

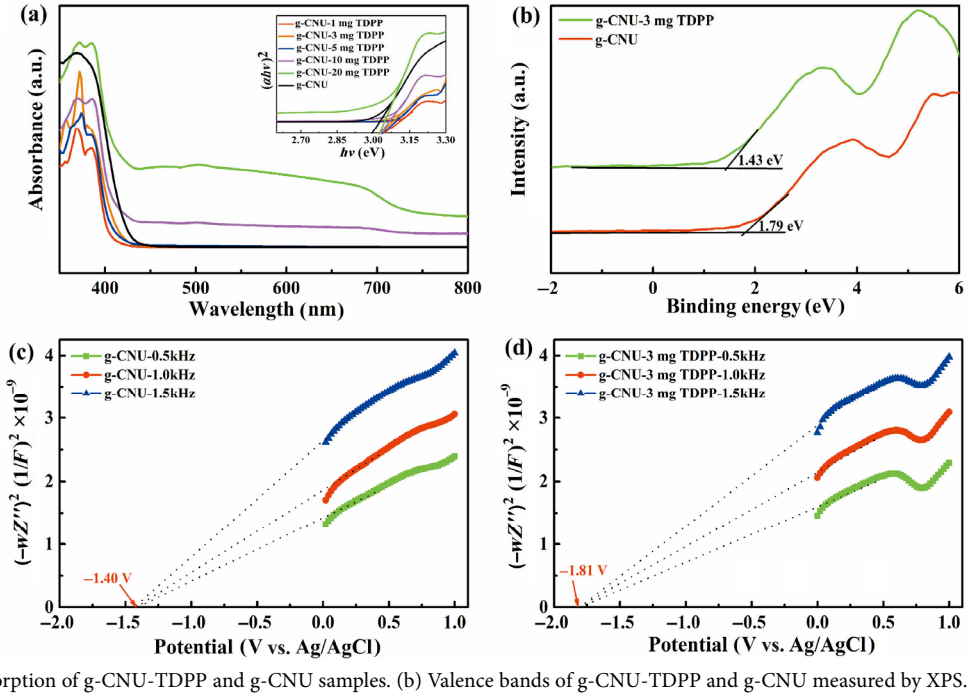

Figure 3 (a) Optical absorption of g-CNU-TDPP and g-CNU samples. (b) Valence bands of g-CNU-TDPP and g-CNU measured by XPS. (c) Mott-Schottky plots of g-CNU. (d) Mott-Schottky plots of g-CNU-TDPP. The inset in (a) is $(\alpha h\nu)^2$ versus $h\nu$ curve of g-CNU-TDPP and g-CNU samples.

derived band gap energies of g-CNU-TDPP and g-CNU were 3.04 and 2.99 eV, matching well with the values calculated from the plots of $(\alpha h\nu)^2$ versus photon energy.

The photoluminescence (PL) spectra showed that the sample g-CNU-TDPP nanosheets exhibited apparently fluorescence quenching (Fig. S6(a) in the ESM), indicating that the recombination rates of the photogenerated charge carriers were greatly inhibited and the separation efficiency was improved. It may be caused by the synergistic effect of the reduced thickness of the nanosheets and molecular heterojunction formed between TDPP and tri-s-triazines units which facilitate the charge carriers transferred to the surface. Furthermore, the slight blue shift of the emission peaks was in good agreement with the observation from UV–Vis absorption spectra. The time-resolved fluorescence decay spectra (Fig. S6(b) in the ESM) showed the reduced fluorescence lifetime of g-CNU-TDPP (4.33 ns) compared with g-CNU (5.74 ns), suggesting another additional non-radiative pathway may be built caused by the doping of TDPP.

The intensity of the Lorentzian line of g-CNU-TDPP (g = 2.003) which was assigned to the unpaired electron of the carbon atoms within aromatic rings was obviously enhanced, comparing to that of g-CNU (Fig. S7 in the ESM). It indicated that the efficiency of exciton splitting and the density of the unpaired electrons was greatly improved in the dark state at room temperature when TDPP embedded into the edges of g-CNU-TDPP nanosheets.

The electrochemical impedance spectra (EIS) measurements (Fig. S8(a) in the ESM) of g-CNU-TDPP showed an evident smaller diameter than that of g-CNU, revealing the weakened charge transfer resistance. Meanwhile, the photoelectrochemical measurements were also carried out to further investigate the charger carriers transportation behaviors. The uniform photocurrent responses (Fig. S8(b) in the ESM) were presented and exhibited good stability, and the enhanced photocurrent density of g-CNU-TDPP proved higher charge carrier separation efficiency when the intramolecular heterojunctions constructed.

3.2 Photocatalytic H_2 evolution performance

Associated with the enlarged specific surface area, more surface catalytic active sites, the expanded visible light absorption range, the enhanced redox ability of photogenerated electrons and the improved charge carriers separation and transportation efficiency, g-CNU-TDPP nanosheets were expected to be excellent candidates for photocatalytic H_2 evolution. The reaction was carried out in aqueous solution using TEOA (10%) as sacrificial agent and using 2 wt.% Pt as cocatalyst. The as-prepared g-CNU-TDPP nanosheets all exhibited distinct enhanced H_2 evolution rate in comparison with pristine g-CNU, especially for the sample g-CNU-3 mg TDPP (Fig. 4(a)). The H_2 evolution rate could reach up to 7.6 $mmol \cdot g^{-1} \cdot h^{-1}$ and was 4-times higher than that of g-CNU. In particular, the evolution rate dropped dramatically when the TDPP content increased to 10 or 20 mg, as we known, the photocatalytic efficiency is not only determined by the absorption ability of the visible light, but also depended on the separation efficiency of the photogenerated electron and holes, too much TDPP incorporation may interrupt the integrity of g-CN matrices and damage the connectivity of g-CN during the process of thermal copolymerization, resulting in the decreased of electron-hole separation efficiency, which explained the samples g-CNU-10 mg TDPP and g-CNU-20 mg TDPP did not exhibit a higher H_2 evolution rate. It can infer that a low doping amount of TDPP was necessary to maintain the excellent photocatalytic performance.

The stability of the photocatalytic H_2 evolution was evaluated by 5 consecutive cycles and each cycle lasted for 5 h (Fig. 4(b)). The H_2 evolution rate was rather stable during the first three cycles, a slight deactivation was noticed in the fourth cycle. When appropriate amount of TEOA was added, the reactivity of H_2 evolution improved again in the fifth run, indicating that the weakened activity was mainly caused by the decreased concentration of TEOA.

The wavelength-dependent AQE of H_2 production were measured using band-pass optical filters. As shown in Fig. 4(c), as to the sample g-CNU, the maximum AQE was 1.9% at 420 nm and there was no H_2 produced when the λ > 475 nm. The H_2 evolution rate of g-CNU-3 mg TDPP exhibited significant increasement over the total range of optical activity comparing with g-CNU and the maximum AQE can reach up to 13.3% at 450 nm. Furthermore, the AQE increased again to 5.2% at 500 nm and kept at 1% at 550 nm, the result is easily to be questioned at first sight as just from the

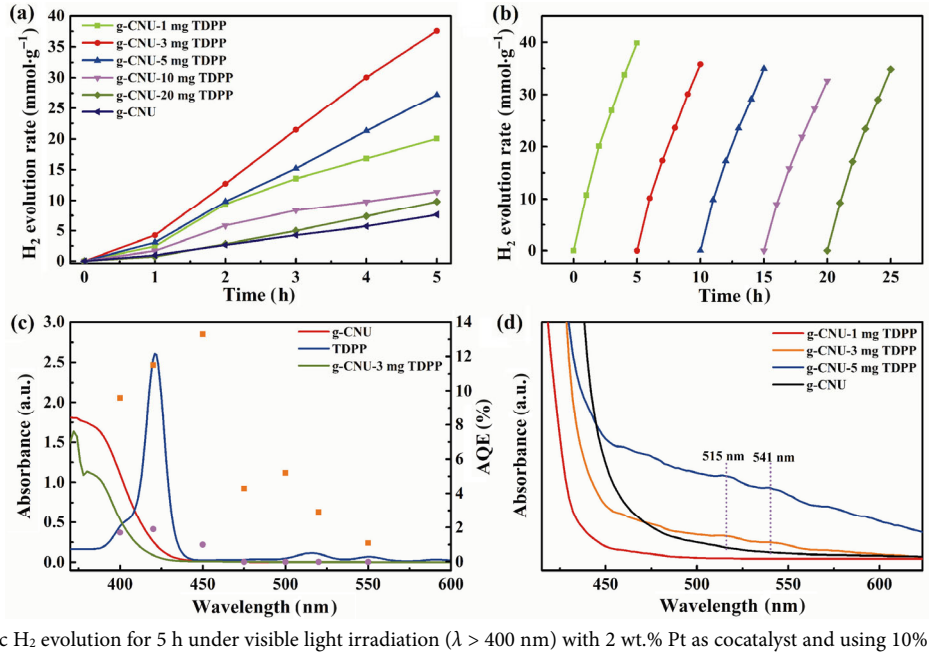

Figure 4 The photocatalytic H_2 evolution for 5 h under visible light irradiation (λ > 400 nm) with 2 wt.% Pt as cocatalyst and using 10% TEOA as sacrificial agent (a) H_2 evolution rate of g-CNU-TDPP and g-CNU samples. (b) Stability analysis of g-CNU-3 mg TDPP with visible light irradiation for 5 cycles and each cycle lasted 5 h. (c) The UV–Vis absorption spectra of TDPP, g-CNU-3 mg TDPP and g-CNU. The AQE of g-CNU-3 mg TDPP and g-CNU under different wavelength irradiation (λ = 365, 400, 420, 450, 475, 500, and 550 nm) with 2 wt.% Pt as cocatalyst and using 10% TEOA as sacrificial agent. ▪ represent the AQE of g-CNU-3 mg TDPP and ● represent the AQE of g-CNU. (d) The partial enlargement of optical absorption of g-CNU-TDPP and g-CNU samples ranged from 400–600 nm.

absorption spectra of g-CNU-3 mg TDPP, it showed no obvious absorption in this wavelength range. While in fact, this result is a good proof that demonstrating that TDPP is not only successfully grafted into the g-CN matrixes but also maintained its original optical absorption capacity at the same time. From the UV–Vis spectra (Fig. 4(c)), TDPP itself has no absorption at 475 nm but the first two Q-band absorption peaks of TDPP start from 495 nm and ended at 567 nm, which explained why the AQE increased again at 500 nm and can still maintain 1% at 550 nm, the experimental data matched well with the partial enlargement of UV–Vis spectra of g-CNU-3 mg TDPP and g-CNU(Fig. 4(d)).

The photocatalyst g-CNU-3 mg TDPP was recovered when the photocatalytic reaction completed and characterized by XRD pattern and FT-IR spectra (Fig. S9 in the ESM). No noticeable change was observed before and after reaction from the XRD and FT-IR spectra, suggesting the excellent stability of g-CNU-3 mg TDPP in photocatalytic reactions.

In order to further understand the electron separation and transfer route, the location of Pt nanoparticles was investigated by TEM image when the photocatalytic reaction finished. As can be seen in Fig. S10(a) in the ESM, Pt particles randomly distributed on the surface of g-CNU nanosheets with the average particle size of 10 nm while they tended to locate at the edges of the g-CNU-TDPP nanosheets with the average size of 2 nm (Figs. S10(b) and S10(c) in the ESM), which again proved TDPP grafting on the edges of g-CNU-TDPP nanosheets and the electrons transferred from tri-s-triazine units to TDPP units where K_2PtCl_6 was *in-situ* reduced to Pt nanoparticles under visible light irradiation.

In combination with the above characterization and experiment results, the possible photocatalytic mechanism and electron transfer routes are speculated as follows (Fig. 5): When TDPP anchored on the edges of the g-CNU-TDPP to construct intramolecular heterojunctions, g-CNU-TDPP could harvest more visible light under the visible light irradiation. The photogenerated electrons and holes could easily transfer to the surface owing to the reduced particle size and thickness of nanosheets and the electrons further transferred to the edges of the nanosheets where TDPP situated because of the energy level matched well between CB of the g-CNU-TDPP and LUMO of TDPP. Pt particles formed by *in-situ* photo-deposition were dispersed on the edges of the nanosheets and acted as cocatalysts to collect electrons to reduce H^+ to H_2. Meanwhile, the photogenerated holes were captured by TEOA. During this process, the synergetic effects of the enlarged specific surface area, the expanded optical absorption range, the enhanced redox capacity of photoinduced electrons and the increased charge carriers separation and transportation efficiency all contributed to the enhanced photocatalytic H_2 evolution performance.

4 Conclusions

In summary, the bottom-up fabrication of porphyrin modified CNNs through covalent bonding has been developed for the first time. The resultant g-CNU-TDPP exhibited excellent photocatalytic H_2 evolution performance with AQE of 13.3% at 450 nm. This methodology can be extended to imbedded metalloporphyrin into the matrices of g-CN where the central metal ions can function as single-site catalytic center, and the as-prepared CNNs modified by metalloporphyrin could be employed in other photocatalytic applications such as CO_2 reduction.

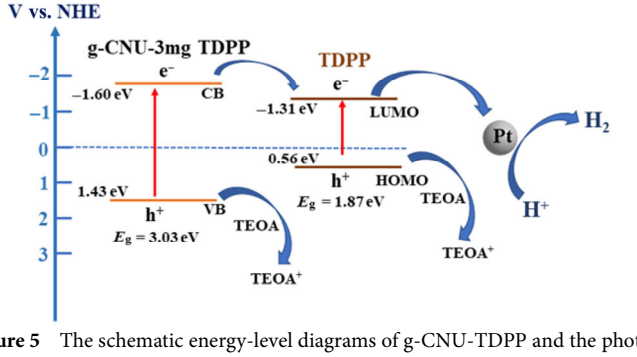

Figure 5 The schematic energy-level diagrams of g-CNU-TDPP and the photo generated charge carriers transfer route at the intramolecular heterojunction interface.

Electronic Supplementary Material: Supplementary material is available in the online version of this article at https://doi.org/10.1007/s12274-019-2562-x.

References

[1] Kudo, A.; Miseki, Y. Heterogeneous photocatalyst materials for water splitting. *Chem. Soc. Rev.* **2009**, *38*, 253–278.

[2] Yang, J. H.; Wang, D. G.; Han, H. X.; Li, C. Roles of cocatalysts in photocatalysis and photoelectrocatalysis. *Acc. Chem. Res.* **2013**, *46*, 1900–1909.

[3] Zong, X.; Yan, H. J.; Wu, G. P.; Ma, G. J.; Wen, F. Y.; Wang, L.; Li, C. Enhancement of photocatalytic H_2 evolution on CdS by loading MoS_2 as cocatalyst under visible light irradiation. *J. Am. Chem. Soc.* **2008**, *130*, 7176–7177.

[4] Xiang, Q. J.; Yu, J. G.; Jaroniec, M. Synergetic effect of MoS_2 and graphene as cocatalysts for enhanced photocatalytic H_2 production activity of TiO_2 nanoparticles. *J. Am. Chem. Soc.* **2012**, *134*, 6575–6578.

[5] Li, Q.; Guo, B. D.; Yu, J. G.; Ran, J. R.; Zhang, B. H.; Yan, H. J.; Gong, J. R. Highly efficient visible-light-driven photocatalytic hydrogen production of CdS-cluster-decorated graphene nanosheets. *J. Am. Chem. Soc.* **2011**, *133*, 10878–10884.

[6] Ran, J. R.; Zhang, J.; Yu, J. G.; Jaroniec, M.; Qiao, S. Z. Earth-abundant cocatalysts for semiconductor-based photocatalytic water splitting. *Chem. Soc. Rev.* **2014**, *43*, 7787–7812.

[7] Tong, X. J.; Cao, X.; Han, T.; Cheong, W. C.; Lin, R.; Chen, Z.; Wang, D. S.; Chen, C.; Peng, Q.; Li, Y. D. Convenient fabrication of BiOBr ultrathin nanosheets with rich oxygen vacancies for photocatalytic selective oxidation of secondary amines. *Nano Res.* **2019**, *12*, 1625–1630.

[8] Wang, X. C.; Maeda, K.; Thomas, A.; Takanabe, K.; Xin, G.; Carlsson, J. M.; Domen, K.; Antonietti, M. A metal-free polymeric photocatalyst for hydrogen production from water under visible light. *Nat. Mater.* **2009**, *8*, 76–80.

[9] Wang, Y.; Wang, X. C.; Antonietti, M. Polymeric graphitic carbon nitride as a heterogeneous organocatalyst: From photochemistry to multipurpose catalysis to sustainable chemistry. *Angew. Chem., Int. Ed.* **2012**, *51*, 68–89.

[10] Ong, W. J.; Tan, L. L.; Ng, Y. H.; Yong, S. T.; Chai, S. P. Graphitic carbon nitride ($g\text{-}C_3N_4$)-based photocatalysts for artificial photosynthesis and environmental remediation: Are we a step closer to achieving sustainability? *Chem. Rev.* **2016**, *116*, 7159–7329.

[11] Volokh, M.; Peng, G. M.; Barrio, J.; Shalom, M. Carbon nitride materials for water splitting photoelectrochemical cells. *Angew. Chem., Int. Ed.* **2019**, *58*, 6138–6151.

[12] Zhou, C.; Shi, R.; Shang, L.; Wu, L. Z.; Tung, C. H.; Zhang, T. R. Template-free large-scale synthesis of $g\text{-}C_3N_4$ microtubes for enhanced visible light-driven photocatalytic H_2 production. *Nano Res.* **2018**, *11*, 3462–3468.

[13] Tang, S. F.; Yin, X. P.; Wang, G. Y.; Lu, X. L.; Lu, T. B. Single titanium-oxide species implanted in 2D $g\text{-}C_3N_4$ matrix as a highly efficient visible-light CO_2 reduction photocatalyst. *Nano Res.* **2019**, *12*, 457–462.

[14] Ma, T. Y.; Ran, J. R.; Dai, S.; Jaroniec, M.; Qiao, S. Z. Phosphorus-doped graphitic carbon nitrides grown *in situ* on carbon-fiber paper: Flexible and reversible oxygen electrodes. *Angew. Chem., Int. Ed.* **2015**, *54*, 4646–4650.

[15] Zhang, P.; Li, X. H.; Shao, C. L.; Liu, Y. C. Hydrothermal synthesis of carbon-rich graphitic carbon nitride nanosheets for photoredox catalysis. *J. Mater. Chem. A* **2015**, *3*, 3281–3284.

[16] Zhang, J. S.; Chen, X. F.; Takanabe, K.; Maeda, K.; Domen, K.; Epping, J. D.; Fu, X. Z.; Antonietti, M.; Wang, X. C. Synthesis of a carbon nitride structure for visible-light catalysis by copolymerization. *Angew. Chem., Int. Ed.* **2010**, *49*, 441–444.

[17] Zhang, J. S.; Zhang, G. G.; Chen, X. F.; Lin, S.; Möhlmann, L.; Dołęga, G.; Lipner, G.; Antonietti, M.; Blechert, S.; Wang, X. C. Co-monomer control of carbon nitride semiconductors to optimize hydrogen evolution with visible light. *Angew. Chem., Int. Ed.* **2012**, *51*, 3183–3187.

[18] Liu, J.; Wang, H. Q.; Chen, Z. P.; Moehwald, H.; Fiechter, S.; Van De Krol, R.; Wen, L. P.; Jiang, L.; Antonietti, M. Microcontact-printing-assisted access of graphitic carbon nitride films with favorable textures toward photoelectrochemical application. *Adv. Mater.* **2015**, *27*, 712–718.
[19] Mane, G. P.; Talapaneni, S. N.; Anand, C.; Varghese, S.; Iwai, H.; Ji, Q. M.; Ariga, K.; Mori, T.; Vinu, A. Preparation of highly ordered nitrogen-containing mesoporous carbon from a gelatin biomolecule and its excellent sensing of acetic acid. *Adv. Funct. Mater.* **2012**, *22*, 3596–3604.
[20] Chen, X. F.; Jun, Y. S.; Takanabe, K.; Maeda, K.; Domen, K.; Fu, X. Z.; Antonietti, M.; Wang, X. C. Ordered mesoporous SBA-15 type graphitic carbon nitride: A semiconductor host structure for photocatalytic hydrogen evolution with visible light. *Chem. Mater.* **2009**, *21*, 4093–4095.
[21] Wang, J. H.; Zhang, C.; Shen, Y. F.; Zhou, Z. X.; Yu, J. C.; Li, Y.; Wei, W.; Liu, S. Q.; Zhang, Y. J. Environment-friendly preparation of porous graphite-phase polymeric carbon nitride using calcium carbonate as templates, and enhanced photoelectrochemical activity. *J. Mater. Chem. A* **2015**, *3*, 5126–5131.
[22] Yan, H. J. Soft-templating synthesis of mesoporous graphitic carbon nitride with enhanced photocatalytic H_2 evolution under visible light. *Chem. Commun.* **2012**, *48*, 3430–3432.
[23] Liang, Q. H.; Li, Z.; Yu, X. L.; Huang, Z. H.; Kang, F. Y.; Yang, Q. H. Macroscopic 3D porous graphitic carbon nitride monolith for enhanced photocatalytic hydrogen evolution. *Adv. Mater.* **2015**, *27*, 4634–4639.
[24] Jun, Y. S.; Lee, E. Z.; Wang, X. C.; Hong, W. H.; Stucky, G. D.; Thomas, A. From melamine-cyanuric acid supramolecular aggregates to carbon nitride hollow spheres. *Adv. Funct. Mater.* **2013**, *23*, 3661–3667.
[25] Shalom, M.; Inal, S.; Fettkenhauer, C.; Neher, D.; Antonietti, M. Improving carbon nitride photocatalysis by supramolecular preorganization of monomers. *J. Am. Chem. Soc.* **2013**, *135*, 7118–7121.
[26] Jordan, T.; Fechler, N.; Xu, J. S.; Brenner, T. J. K.; Antonietti, M.; Shalom, M. "Caffeine doping" of carbon/nitrogen-based organic catalysts: Caffeine as a supramolecular edge modifier for the synthesis of photoactive carbon nitride tubes. *ChemCatChem* **2015**, *7*, 2826–2830.
[27] Zhang, J. S.; Chen, Y.; Wang, X. C. Two-dimensional covalent carbon nitride nanosheets: Synthesis, functionalization, and applications. *Energy Environ. Sci.* **2015**, *8*, 3092–3108.
[28] Liu, Q.; Chen, T. X.; Guo, Y. R.; Zhang, Z. G.; Fang, X. M. Ultrathin g-C_3N_4 nanosheets coupled with carbon nanodots as 2D/0D composites for efficient photocatalytic H_2 evolution. *Appl. Catal. B: Environ.* **2016**, *193*, 248–258.
[29] Yang, S. S.; Gong, Y. J.; Zhang, J. S.; Zhan, L.; Ma, L. L.; Fang, Z. Y.; Vajtai, R.; Wang, X. C.; Ajayan, P. M. Exfoliated graphitic carbon nitride nanosheets as efficient catalysts for hydrogen evolution under visible light. *Adv. Mater.* **2013**, *25*, 2452–2456.
[30] Han, C.; Wang, Y. D.; Lei, Y. P.; Wang, B.; Wu, N.; Shi, Q.; Li, Q. *In situ* synthesis of graphitic-C_3N_4 nanosheet hybridized N-doped TiO_2 nanofibers for efficient photocatalytic H_2 production and degradation. *Nano Res.* **2015**, *8*, 1199–1209.
[31] Ding, J.; Liu, Q. Q.; Zhang, Z. Y.; Liu, X.; Zhao, J. Q.; Cheng, S. B.; Zong, B. N.; Dai, W. L. Carbon nitride nanosheets decorated with WO_3 nanorods: Ultrasonic-assisted facile synthesis and catalytic application in the green manufacture of dialdehydes. *Appl. Catal. B: Environ.* **2015**, *165*, 511–518.
[32] Shan, W. J.; Hu, Y.; Bai, Z. G.; Zheng, M. M.; Wei, C. H. *In situ* preparation of g-C_3N_4/bismuth-based oxide nanocomposites with enhanced photocatalytic activity. *Appl. Catal. B: Environ.* **2016**, *188*, 1–12.
[33] Wang, Y. Y.; Jiang, W. J.; Luo, W. J.; Chen, X. J.; Zhu, Y. F. Ultrathin nanosheets g-C_3N_4@Bi_2WO_6 core-shell structure via low temperature reassembled strategy to promote photocatalytic activity. *Appl. Catal. B: Environ.* **2018**, *237*, 633–640.
[34] Shiraishi, Y.; Kofuji, Y.; Kanazawa, S.; Sakamoto, H.; Ichikawa, S.; Tanaka, S.; Hirai, T. Platinum nanoparticles strongly associated with graphitic carbon nitride as efficient co-catalysts for photocatalytic hydrogen evolution under visible light. *Chem. Commun.* **2014**, *50*, 15255–15258.
[35] Cheng, N. Y.; Tian, J. Q.; Liu, Q.; Ge, C. J.; Qusti, A. H.; Asiri, A. M.; Al-Youbi, A. O.; Sun, X. P. Au-nanoparticle-loaded graphitic carbon nitride nanosheets: Green photocatalytic synthesis and application toward the degradation of organic pollutants. *ACS Appl. Mater. Interfaces* **2013**, *5*, 6815–6819.
[36] Zhang, X. B.; Lian, C.; Chen, Z.; Chen, C.; Li, Y. D. Preparation of freestanding palladium nanosheets modified with gold nanoparticles at edges. *Nano Res.* **2018**, *11*, 4142–4148.
[37] Hu, M. Z.; Zhang, J.; Zhu, W.; Chen, Z.; Gao, X.; Du, X. J.; Wan, J. W.; Zhou, K. B.; Chen, C.; Li, Y. D. 50 ppm of Pd dispersed on $Ni(OH)_2$ nanosheets catalyzing semi-hydrogenation of acetylene with high activity and selectivity. *Nano Res.* **2018**, *11*, 905–912.
[38] Lu, X. L.; Xu, K.; Chen, P. Z.; Jia, K. C.; Liu, S.; Wu, C. Z. Facile one step method realizing scalable production of g-C_3N_4 nanosheets and study of their photocatalytic H_2 evolution activity. *J. Mater. Chem. A* **2014**, *2*, 18924–18928.
[39] Xu, J.; Zhang, L. W.; Shi, R.; Zhu, Y. F. Chemical exfoliation of graphitic carbon nitride for efficient heterogeneous photocatalysis. *J. Mater. Chem. A* **2013**, *1*, 14766–14772.
[40] Zhang, X. D.; Xie, X.; Wang, H.; Zhang, J. J.; Pan, B. C.; Xie, Y. Enhanced photoresponsive ultrathin graphitic-phase C_3N_4 nanosheets for bioimaging. *J. Am. Chem. Soc.* **2013**, *135*, 18–21.
[41] Dong, F.; Wu, L. W.; Sun, Y. J.; Fu, M.; Wu, Z. B.; Lee, S. C. Efficient synthesis of polymeric g-C_3N_4 layered materials as novel efficient visible light driven photocatalysts. *J. Mater. Chem.* **2011**, *21*, 15171–15174.
[42] Liu, J. H.; Zhang, T. K.; Wang, Z. C.; Dawson, G.; Chen, W. Simple pyrolysis of urea into graphitic carbon nitride with recyclable adsorption and photocatalytic activity. *J. Mater. Chem.* **2011**, *21*, 14398–14401.
[43] Zhang, G. G.; Zhang, J. S.; Zhang, M. W.; Wang, X. C. Polycondensation of thiourea into carbon nitride semiconductors as visible light photocatalysts. *J. Mater. Chem.* **2012**, *22*, 8083–8091.
[44] Wu, M.; Yan, J. M.; Tang, X. N.; Zhao, M.; Jiang, Q. Synthesis of potassium-modified graphitic carbon nitride with high photocatalytic activity for hydrogen evolution. *ChemSusChem* **2014**, *7*, 2654–2658.
[45] Zhang, N.; Wang, L.; Wang, H. M.; Cao, R. H.; Wang, J. F.; Bai, F.; Fan, H. Y. Self-assembled one-dimensional porphyrin nanostructures with enhanced photocatalytic hydrogen generation. *Nano Lett.* **2018**, *18*, 560–566.
[46] Wu, K. L.; Chen, X.; Liu, S. J.; Pan, Y.; Cheong, W. C.; Zhu, W.; Cao, X.; Shen, R. A.; Chen, W. X.; Luo, J. et al. Porphyrin-like Fe-N_4 sites with sulfur adjustment on hierarchical porous carbon for different rate-determining steps in oxygen reduction reaction. *Nano Res.* **2018**, *11*, 6260–6269.
[47] Bonin, J.; Robert, M.; Routier, M. Selective and efficient photocatalytic CO_2 reduction to CO using visible light and an iron-based homogeneous catalyst. *J. Am. Chem. Soc.* **2014**, *136*, 16768–16771.
[48] Knör, G. Photocatalytic reactions of porphyrin-based multielectron transfer sensitizers. *Coord. Chem. Rev.* **1998**, *171*, 61–70.
[49] Rao, H.; Lim, C. H.; Bonin, J.; Miyake, G. M.; Robert, M. Visible-light-driven conversion of CO_2 to CH_4 with an organic sensitizer and an iron porphyrin catalyst. *J. Am. Chem. Soc.* **2018**, *140*, 17830–17834.
[50] Chen, D. M.; Wang, K. W.; Hong, W. Z.; Zong, R. L.; Yao, W. Q.; Zhu, Y. F. Visible light photoactivity enhancement via CuTCPP hybridized g-C_3N_4 nanocomposite. *Appl. Catal. B: Environ.* **2015**, *166–167*, 366–373.
[51] Zhao, G. X.; Pang, H.; Liu, G. G.; Li, P.; Liu, H. M.; Zhang, H. B.; Shi, L.; Ye, J. H. Co-porphyrin/carbon nitride hybrids for improved photocatalytic CO_2 reduction under visible light. *Appl. Catal. B: Environ.* **2017**, *200*, 141–149.
[52] Liu, J. B.; Shi, H. J.; Shen, Q.; Guo, C. Y.; Zhao, G. H. A biomimetic photoelectrocatalyst of Co-porphyrin combined with a g-C_3N_4 nanosheet based on π-π supramolecular interaction for high-efficiency CO_2 reduction in water medium. *Green Chem.* **2017**, *19*, 5900–5910.
[53] Lin, L.; Hou, C. C.; Zhang, X. H.; Wang, Y. J.; Chen, Y.; He, T. Highly efficient visible-light driven photocatalytic reduction of CO_2 over g-C_3N4 nanosheets/tetra(4-carboxyphenyl)porphyrin iron(III) chloride heterogeneous catalysts. *Appl. Catal. B: Environ.* **2018**, *221*, 312–319.
[54] Da Silva, E. S.; Moura, N. M. M.; Neves, M. G. P. M. S.; Coutinho, A.; Prieto, M.; Silva, C. G.; Faria, J. L. Novel hybrids of graphitic carbon nitride sensitized with *free-base* meso-tetrakis(carboxyphenyl) porphyrins for efficient visible light photocatalytic hydrogen production. *Appl. Catal. B: Environ.* **2018**, *221*, 56–69.
[55] Wang, D. H.; Pan, J. N.; Li, H. H.; Liu, J. J.; Wang, Y. B.; Kang, L. T.; Yao, J. N. A pure organic heterostructure of μ-oxo dimeric iron(III) porphyrin and graphitic-C_3N_4 for solar H_2 roduction from water. *J. Mater. Chem. A* **2016**, *4*, 290–296.
[56] Qu, D.; Liu, J.; Miao, X.; Han, M. M.; Zhang, H. C.; Cui, Z.; Sun, S. R.; Kang, Z. H.; Fan, H. Y.; Sun, Z. C. Peering into water splitting mechanism of g-C_3N_4-carbon dots metal-free photocatalyst. *Appl. Catal. B: Environ.* **2018**, *227*, 418–424.
[57] Zhang, Y. W.; Liu, J. H.; Wu, G.; Chen, W. Porous graphitic carbon nitride synthesized via direct polymerization of urea for efficient sunlight-driven photocatalytic hydrogen production. *Nanoscale* **2012**, *4*, 5300–5303.
[58] Yang, W.; Yang, F.; Hu, T. L.; King, S. C.; Wang, H. L.; Wu, H.; Zhou, W.; Li, J. R.; Arman, H. D.; Chen, B. Microporous diaminotriazine-decorated porphyrin-based hydrogen-bonded organic framework: Permanent porosity and proton conduction. *Cryst. Growth Des.* **2016**, *16*, 5831–5835.